



# Heterostructured simple perovskite nanorod-decorated double perovskite cathode for solid oxide fuel cells: Highly catalytic activity, stability and CO<sub>2</sub>-durability for oxygen reduction reaction

Feifei Lu<sup>a</sup>, Tian Xia<sup>a,\*</sup>, Qiang Li<sup>a</sup>, Jingping Wang<sup>b</sup>, Lihua Huo<sup>a</sup>, Hui Zhao<sup>a,\*</sup>

<sup>a</sup> Key Laboratory of Functional Inorganic Materials Chemistry, Ministry of Education, School of Chemistry, Chemical Engineering and Materials, Heilongjiang University, Harbin, 150080, People's Republic of China

<sup>b</sup> Key Laboratory of Superlight Material and Surface Technology, Ministry of Education, College of Materials Science and Chemical Engineering, Harbin Engineering University, Harbin, 150001, People's Republic of China



## ARTICLE INFO

### Keywords:

*In situ* exsolution  
Heterostructured materials  
Simple perovskite-double perovskite  
Intermediate-temperature solid oxide fuel cells  
Catalytic oxygen reduction reaction activity

## ABSTRACT

Apart from conventional composite materials, *in situ* exsolution for constructing the heterostructure is one of the most effective strategies to design the high-performance electro-catalysts. Herein we report a novel heterostructured simple perovskite nanorod-decorated A site-deficient double perovskite  $\text{PrBa}_{0.94}\text{Co}_2\text{O}_{5+\delta}$  (SPN-A-PBC) cathode, synthesized by an *in situ* exsolving process from A site-deficient double perovskite  $\text{PrBa}_{0.94}\text{Co}_2\text{O}_{5+\delta}$  (A-PBC). The results demonstrate a highly electro-catalytic activity of the SPN-A-PBC cathode toward oxygen reduction reaction (ORR) for intermediate-temperature solid oxide fuel cells (IT-SOFCs), achieving a very low and stable polarization resistance of  $\sim 0.025 \Omega \text{ cm}^2$  at 700 °C in air. The anode-supported single cell with this heterostructured cathode delivers a maximum power density of  $1.1 \text{ W cm}^{-2}$  at 700 °C and a superior steady operation over 120 h at a loading voltage of 0.6 V. Furthermore, the SPN-A-PBC electrode exhibits a good tolerance to CO<sub>2</sub>. When tested in air with 6 vol% CO<sub>2</sub> at 700 °C, the SPN-A-PBC electrode still maintains a stable polarization resistance of  $\sim 0.078 \Omega \text{ cm}^2$ . The unique catalytic activity of the SPN-A-PBC cathode for ORR may be attributed to extended active sites, abundant interface defects, enhanced redox property and oxygen mobility. The fast ORR kinetics and excellent durability in air with CO<sub>2</sub> highlight the potential of SPN-A-PBC as a potential functional material in the energy conversion devices.

## 1. Introduction

With growing energy conversion demand and environmental issue, the clean and direct conversion from renewable source to electric power has attracted much attention on the sustainable development in the future [1]. As the third-generation fuel cell technology, tremendous work has been focused on solid oxide fuel cells (SOFCs) in the past several decades due to their high conversion efficiency without Carnot cycling limitation, low pollution emission (H<sub>2</sub>O and CO<sub>2</sub> etc.), negligible noise level and excellent fuel flexibility [2,3]. To advance the commercial progress of SOFCs in various fields, the operating temperature should be located in the intermediate temperature range (500–750 °C), which makes the choice of less expensive materials and shortens the start-up time [4,5]. Some new applications would be opened, such as heating and power union, automotive devices and even portable electronics [6]. For designing intermediate-temperature solid oxide fuel cells (IT-SOFCs), one of the most important factors is the

selection of high-performance electro-catalysts toward oxygen reduction reaction (ORR) with sufficient long-term stability. Therefore, the considerable efforts have been devoted on the conventional perovskite (ABO<sub>3</sub>) and K<sub>2</sub>NiF<sub>4</sub>-type oxides as the cathode materials for IT-SOFCs, such as La<sub>0.6</sub>Sr<sub>0.4</sub>Co<sub>0.2</sub>Fe<sub>0.8</sub>O<sub>3-δ</sub> (LSCF), Ba<sub>0.5</sub>Sr<sub>0.5</sub>Co<sub>0.8</sub>Fe<sub>0.2</sub>O<sub>3-δ</sub> (BSCF), doped SrCoO<sub>3-δ</sub> (SC) and La<sub>2</sub>NiO<sub>4</sub> (LNO) etc., showing an attractive catalytic activity at reduced temperatures [7–11]. However, the practical application is still limited by their poor chemical stability, e. g., BSCF suffers a decomposition into the Ba-rich hexagonal phase [12]. On the other hand, the Ba/Sr-enrichment may induce the formation of secondary phases, leading to an unfavourable durability with a gradual decay in the electrode performance due to CO<sub>2</sub> poisoning effect [13–15]. Up to now, there remains a challenge to explore an alternative candidate that meets the practical requirements of the cathode for IT-SOFCs.

In recent years, layered double perovskite  $\text{PrBaCo}_2\text{O}_{5+\delta}$  has been considered as a potential cathode material for IT-SOFCs because of

\* Corresponding authors.

E-mail addresses: [xitian@hlju.edu.cn](mailto:xitian@hlju.edu.cn) (T. Xia), [zhaoxu98@hlju.edu.cn](mailto:zhaoxu98@hlju.edu.cn) (H. Zhao).

adequate mixed ionic and electronic conductivity, high oxygen surface exchange and diffusion coefficients [16–18]. Especially,  $\text{PrBaCo}_2\text{O}_{5+\delta}$  balances a low oxygen Frenkel energy (0.24 eV per defect) with an appreciable antisite energy (~1 eV), which is beneficial for oxygen mobile in the bulk electrode [19]. To further optimize the electrochemical performance, two classic approaches are presented in the previous publications: one is the substitution of alkaline earth/lanthanide earth or transition metal ions for A- or B-site cations [20–22]; another is to introducing the electrolyte component into PBC, such as  $\text{Ce}_{0.9}\text{Gd}_{0.1}\text{O}_{1.95}$  (CGO) and  $\text{Ce}_{0.8}\text{Sm}_{0.2}\text{O}_{1.9}$  (SDC) [23,24]. Unlike a single-phase compound, the composite materials hold the synergistic effects on the electro-catalytic properties from two distinct components. This concept might be extended for developing the novel heterostructured cathodes. The heterostructured perovskite oxides coupled with a nanoscale metal or oxide catalyst have been evaluated as potential cathodes for IT-SOFCs, such as Ag nanoparticle-decorated  $\text{Sr}_{0.95}\text{Ag}_{0.05}\text{Nb}_{0.1}\text{Co}_{0.9}\text{O}_{3-\delta}$  [25],  $\text{La}_{0.85}\text{Sr}_{0.15}\text{MnO}_{3-\delta}$ -decorated LSCF [26], “Sr”-decorated  $\text{La}_{0.6}\text{Sr}_{0.4}\text{CoO}_{3-\delta}$  [27],  $\text{Sm}_{0.5}\text{Sr}_{0.5}\text{CoO}_3$ -decorated CGO [28],  $\text{Nd}_{0.5}\text{Sr}_{0.5}\text{CoO}_{3-\delta}/\text{Nd}_{0.8}\text{Sr}_{1.2}\text{CoO}_{4+\delta}$  heterointerfaces [29], and so forth. However, the complicated synthesis procedure, special apparatus and extreme experimental condition are often required for preparing the heterostructured materials, including the direct-current sputtering, pulsed laser deposition, vacuum-free infiltration and subsequent freeze-drying combustion, which makes it difficult to be cost-effectively prepared with a large scale.

With respect to heterostructured double perovskites, MnO nanoparticles-decorated  $\text{NdBaMn}_2\text{O}_{5+\delta}$  has been reported first, undergoing a phase transition from simple perovskite  $\text{Nd}_{0.5}\text{Ba}_{0.5}\text{MnO}_{3-\delta}$  to double perovskite  $\text{NdBaMn}_2\text{O}_{5+\delta}$  under high-temperature reducing condition [30]. Hua et al. also reported the heterostructured  $\text{Co}/\text{CoO}_x/(\text{PrBa}_{0.8}\text{Ca}_{0.2})_{0.95}(\text{Co}_{1.5}\text{Fe}_{0.5})_{0.95}\text{Co}_{0.05}\text{O}_{5+\delta}$  nanofibres [31], and concluded that A-site deficiency in the perovskite oxides can enable the exsolution of metal or oxide nanoparticles from the host lattice [32]. The cation-stoichiometric perovskite is thermodynamically more stable than A-site deficient one, thereby leading to a strong exsolving force of B-site atoms. Consequently, A-site deficiency strategy has been suggested to be a choice to establish the nanoparticle-decorated double perovskite composites.

Herein we report a novel heterostructured simple perovskite nanorod-decorated A site-deficient double perovskite  $\text{PrBa}_{0.94}\text{Co}_2\text{O}_{5+\delta}$  (SPN-A-PBC) cathode, evaluated as a high-performance and stable electro-catalyst for ORR at intermediate temperatures. This heterostructure is prepared by a facile *in situ* exsolving technique from A site-deficient double perovskite  $\text{PrBa}_{0.94}\text{Co}_2\text{O}_{5+\delta}$  (A-PBC). In such heterostructure, the simple perovskite nanorods (SPNs) are toughly anchored on the surface of A-PBC. The SPN-A-PBC cathode exhibits a high catalytic activity for ORR, as evidenced by low polarization resistance and high maximum power density. Moreover, the SPN-A-PBC cathode possesses an excellent  $\text{CO}_2$ -durability.

## 2. Experimental

### 2.1. Synthesis of material and fabrication of cell

For the preparation of heterostructured SPN-A-PBC electrode, A site-deficient double perovskite  $\text{PrBa}_{0.94}\text{Co}_2\text{O}_{5+\delta}$  oxide has been synthesized as the precursor by a conventional solid-state ceramic reaction. The raw  $\text{Pr}_6\text{O}_{11}$  was pre-heated at 1000 °C overnight to remove the adsorbed carbonates and hydrates. Typically, stoichiometric amounts of  $\text{Pr}_6\text{O}_{11}$  (Shanghai Yuelong New Materials Co. Ltd., 99.99%),  $\text{BaCO}_3$  (Tianjin Kemiou Chemicals Co. Ltd., > 99%) and  $\text{Co}_2\text{O}_3$  (Tianjin Guangfu Co. Ltd., > 99%) powders were mixed and ground for 40 min using dehydrated ethanol as powder dispersant, and then put into a muffle furnace and calcined at 1050 °C for 12 h in air with a heating ramp of 5 °C min<sup>-1</sup>, followed by naturally cooling down to room temperature. The resulting product was denoted as PBC-1.

Subsequently, the as-synthesized PBC-1 powder (0.1 g) was mixed homogeneously with 0.3 mL of terpineol (Tianjin Kemiou Chemicals Co. Ltd., analytical purity) containing 3 wt % of ethyl cellulose (Shanghai Sinopharm Chemicals Co. Ltd., analytical purity) to form an electrode ink. This ink was painted onto both sides of as-sintered  $\text{Ce}_{0.9}\text{Gd}_{0.1}\text{O}_{1.95}$  (CGO) electrolyte substrate, and then calcined at 950 °C for 6 h in air to fabricate a symmetric half-cell with the SPN-A-PBC electrode. The effective electrode area for the symmetric cell was 0.25 cm<sup>2</sup>. The CGO electrolyte substrates (~12 mm in diameter and ~1 mm in thickness) were prepared by pressing the commercial CGO powder (Ningbo SOFCMAN ENERGY TECHNOLOGY Co. Ltd.) into the pellets at 18 MPa and then sintering at 1200 °C for 24 h and 1400 °C for 12 h in air.

In order to be compared with the single A-PBC electrode, the  $\text{PrBa}_{0.94}\text{Co}_2\text{O}_{5+\delta}$  sample denoted as PBC-2 has been synthesized at 1000 °C for 12 h in air by a solid-state reaction using same agents  $\text{Pr}_6\text{O}_{11}$ ,  $\text{BaCO}_3$  and  $\text{Co}_2\text{O}_3$  as starting materials. The electrode ink was prepared by mixing 0.1 g of PBC-2 with terpineol containing 3 wt % of ethyl cellulose (0.3 mL), and then painted onto both sides of the CGO substrate. Finally, the symmetric cell with the A-PBC electrode was acquired after calcining at 950 °C for 6 h in air.

The anode-supported single cells with a  $\text{Ni-Zr}_{0.85}\text{Y}_{0.15}\text{O}_{1.93}$  (YSZ) anode, a YSZ electrolyte, a CGO buffer layer and the SPN-A-PBC (A-PBC) cathode were fabricated for fuel cell tests. The half-cells with a configuration of  $\text{Ni-YSZ}|\text{YSZ}|\text{CGO}$  were fabricated by a screen-printing technique (Ningbo SOFCMAN ENERGY TECHNOLOGY Co. Ltd.). The as-synthesized PBC-1 (PBC-2) powder was mixed homogeneously with terpineol containing 3 wt % of ethyl cellulose to prepare the cathode ink. This ink was painted onto the CGO buffer layer with a surface area of 0.25 cm<sup>2</sup>, and then calcined at 950 °C for 6 h in air to fabricate the SPN-A-PBC (A-PBC) cathode.

### 2.2. Characterization

Room-temperature X-ray diffraction (XRD) was conducted on a BRUKER diffractometer (AXS D8 Advance) with  $\text{Cu K}_\alpha$  radiation ( $\lambda = 0.15418$  nm). The data was collected in a 2θ range of 10–80° with scanning step of 0.02°. The experimental XRD profiles were analyzed by Rietveld refinement using Materials Studio (MS) software. Field-emission scanning electron microscopy (SEM, Hitachi S4800) was employed to observe the microstructure of the sample at an accelerating voltage of 10 kV. Transition electron microscopy (TEM), high-resolution transition electron microscopy (HRTEM), selected-area electron diffraction (SAED), high-angle annular dark field scanning transmission electron microscopy (HAADF-STEM) equipped with energy-dispersive X-ray spectroscopy (EDX) were performed with an instrument (FEI Tecnai G2 S-Twin) with an electron gun operated at 200 kV. X-ray photoelectron spectroscopy (XPS) was carried out with an AXIS Ultra DLD spectrometer (UK, KRATOS) with monochromatic  $\text{Al K}_\alpha$  radiation (1486.6 eV). The base pressure of the instrument was set to  $7 \times 10^{-8}$  Pa, and the data was calibrated by the binding energy of C 1s (284.8 eV) and fitted with XPSPEAK software. Nitrogen adsorption-desorption isotherms were obtained in a Micromeritics ASAP 2420 system at 77.4 K. The specific surface area was calculated by the Brunauer-Emmett-Teller (BET) method.

Two programmed temperature measurements, hydrogen-temperature-programmed reduction ( $\text{H}_2$ -TPR) and oxygen-temperature-programmed desorption ( $\text{O}_2$ -TPD), were applied to evaluate the redox property and the oxygen mobility of the samples.  $\text{H}_2$ -TPR and  $\text{O}_2$ -TPD were performed with a chemisorption analyzer (Tianjin XIANQUAN, TP5080). Prior to the experiments, the samples were pre-heated at 300 °C for 1 h in a flowing  $\text{O}_2$  atmosphere with a flow rate of 30 mL min<sup>-1</sup> to remove the possible contaminants on the surface of the sample, and then cooled down to room temperature. In  $\text{O}_2$ -TPD experiments, approximate 100 mg sample was heated up to 900 °C with a heating rate of 10 °C min<sup>-1</sup> in pure He (30 mL min<sup>-1</sup>). In  $\text{H}_2$ -TPR experiments,

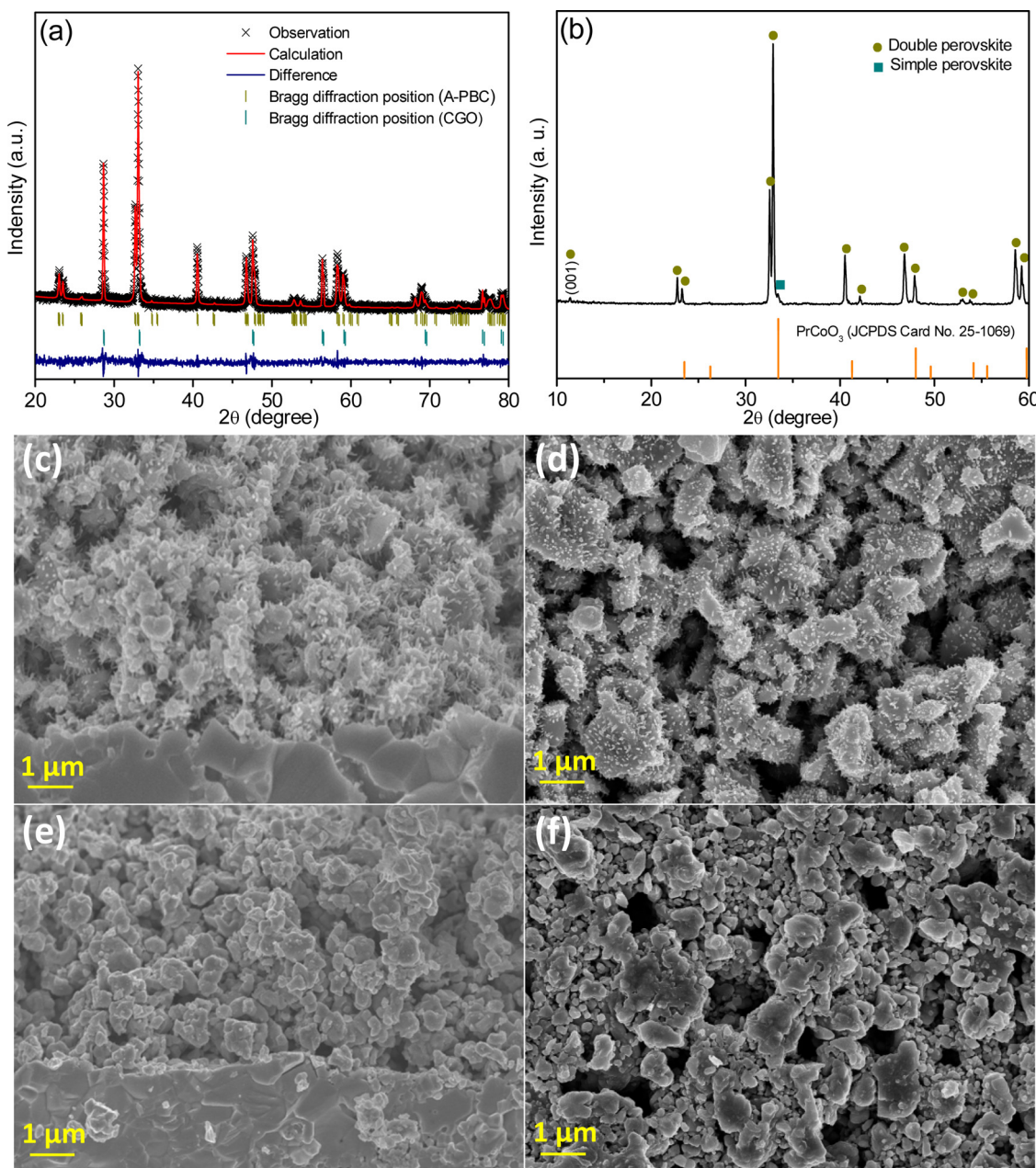


**Fig. 1.** (a) XRD pattern (crosses) of the SPN-A-PBC electrode deposited on a CGO substrate after calcining at 950 °C for 6 h in air. The continuous curve through crosses is the calculated pattern, the vertical markers shows the Bragg peak positions expected in the structure, and a line beneath the patterns represents the difference between the observed pattern and that calculated in the refinement analysis. (b) XRD pattern of the SPN-A-PBC sample after calcining at 950 °C for 6 h without CGO substrate. (c) Cross and (d) surface-section view of SEM images of the SPN-A-PBC electrode on a CGO substrate. (e) Cross and (f) surface-section view of SEM images of the A-PBC electrode on a CGO substrate.

approximate 20 mg sample was placed in a quartz reactor and heated up to 900 °C with a heating ramp of 10 °C min<sup>-1</sup> in a 5 vol% H<sub>2</sub>/N<sub>2</sub> gas mixture (30 mL min<sup>-1</sup>). The amount of consumed H<sub>2</sub> was calculated from the integrated peak area using CuO as a referenced standard.

### 2.3. Electrochemical measurement

Electrochemical impedance spectroscopy (EIS) was measured on the symmetric half-cells using an electrochemical workstation (AUTOLAB PROSTAT30). The measurements were carried out from 500 °C to 700 °C in air, in a frequency range of 10<sup>-2</sup>–10<sup>6</sup> Hz with AC amplitude of 10 mV. For the CO<sub>2</sub>-durability test, the impedance spectra were recorded initially as a function of time at 700 °C in air with different concentrations of CO<sub>2</sub> (1, 4, 6 and 10 vol %), and the air atmosphere

was recovered finally. The impedance spectra were also measured as a function of oxygen partial pressure (pO<sub>2</sub>) to explore the different steps of ORR involved in the polarization resistance (R<sub>p</sub>). The various pO<sub>2</sub> values were controlled by mixing high-purity N<sub>2</sub> (99.99%) and O<sub>2</sub> (99.99%) and monitored by an oxygen sensor. The impedance data was fitted by the equivalent circuits using Zview2 software. All of raw impedance spectra multiply by S/2, in order to normalize by surface area (S) of the electrode. The single cells were fixed and sealed onto an alumina tube with a ceramic adhesive (Aremco, Cerama bond 552). The humidified H<sub>2</sub> (3% H<sub>2</sub>O/97% H<sub>2</sub>) with a flow rate of 50 mL min<sup>-1</sup> and ambient air was supplied as the fuel and the oxidant, respectively. The voltage (V) and power density (P) were recorded as a function of current density (I) on an electrochemical workstation (AUTOLAB PROSTAT302 N). Before fuel cell tests, the single cells were heated at

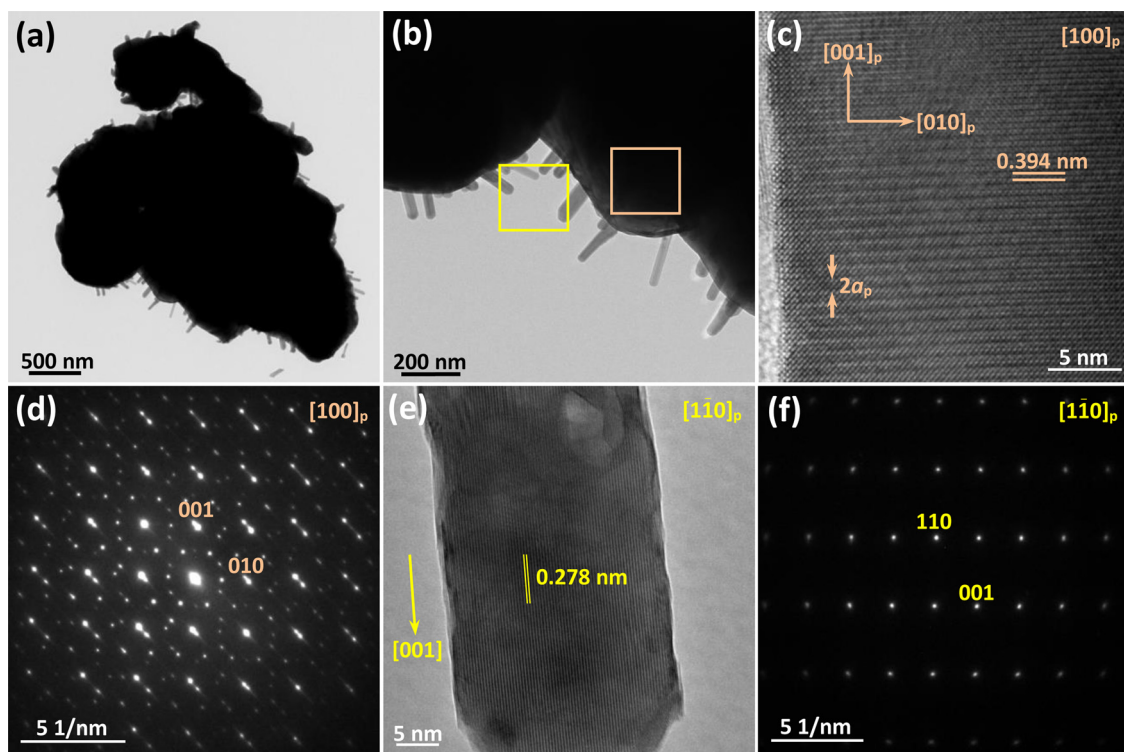


**Fig. 2.** (a) Representative low-magnification and (b) high-magnification TEM images of the SPN-A-PBC sample. (c) HRTEM image and (d) SAED pattern of an A-PBC crystal taken from orange square region in Fig. 2b. (e) HRTEM image and (f) SAED pattern of an individual SPN taken from yellow square region in Fig. 2b (For interpretation of the references to colour in this figure legend, the reader is referred to the web version of this article).

700 °C for 30 min to reduce the NiO component into the metallic Ni.

### 3. Results and discussion

#### 3.1. Structure, morphology and phase composition of the SPN-A-PBC electrocatalyst

As we know, the main rate-limiting step of ORR for many perovskite-type cathodes is the relatively slow oxygen surface exchange kinetics. Therefore, the surface modification of these cathodes with highly active electro-catalysts, namely the interfacial heterostructure, may efficiently improve the electro-catalytic ORR activity. We have demonstrated that layered double perovskites have a high catalytic ORR activity at reduced temperatures [33], while the simple perovskite oxides with high symmetry are also considered to be the good electro-catalysts for ORR [34,35]. It is believed that the heterostructured simple perovskite/layered double perovskite materials may show the unique electrochemical properties [31,36].

In this study, a facile *in situ* exsolving method is developed for preparing the heterostructured SPN-A-PBC cathode from the pristine A-PBC precursor. The A-PBC precursor (PBC-1) shows a single phase composition without any detected impurities (Fig. S1). To go insight into accuracy structure, Rietveld refinement is adopted for fitting the experimental profile, which can be indexed using a tetragonal space group *P4/mmm* and a unit cell  $a_p \times a_p \times 2a_p$  characteristic of layered-type double perovskite ( $a_p$  refers to the lattice parameter of an ideal cubic perovskite). The refinement converges to the lattice parameters of  $a = b = 0.39040$  and  $c = 0.76341$  nm, with a weight-profile  $R_{wp}$  factor of 3.59% and a profile-fitting  $R_p$  factor of 2.81% (Fig. S1), similar to other reports on  $\text{PrBaCo}_2\text{O}_{5+\delta}$  annealed in air [21,37]. The layered doubling structure of A-PBC is further confirmed by HRTEM and fast Fourier transformation (FFT) pattern. Fig. S2a shows the HRTEM image of the PBC-1 sample along the  $[100]_p$  zone axis. The contrast difference in HRTEM image is consistent with the intensity line-profile running

along the  $[001]_p$  direction, as shown in Fig. S2b. The high-intensity peaks correspond to the cation ( $\text{Pr/Ba}$ ) columns, and the oxygen columns are indicated by other low-intensity ones, suggesting the layer-type ordering of atoms with a  $2a_p$  periodicity along the  $[001]_p$  direction. This ordering is ascribed to the  $[\text{Pr-O}]$  layer alternating with the  $[\text{Ba-O}]$  layer in A-PBC. The corresponding FFT pattern is shown as the inset of Fig. S2a, and can be indexed on a tetragonal structure with two-fold superlattice reflections along the  $[001]_p$  direction.

The heterostructured SPN-A-PBC electrode is fabricated by depositing the PBC-1 sample on a CGO substrate at 950 °C for 6 h in air. Fig. 1a shows the XRD pattern of the SPN-A-PBC electrode with a CGO substrate. Two different phases from A-PBC and CGO can be clearly identified. Rietveld refinement is performed in the space group *P4/mmm* and *Fm-3m* for A-PBC and CGO, respectively. The refined results are also shown in Fig. 1a, which gives the reliable factors of  $R_{wp} = 8.09\%$  and  $R_p = 6.29\%$ . The exsolved SPNs cannot be detected in this stage due to their low content. In order to identify the SPN composite, the PBC-1 in. is directly calcined at 950 °C for 6 h in air without CGO substrate. The corresponding XRD pattern between 10° and 60° is shown in Fig. 1b. A small new diffraction peak considered to represent a simple perovskite  $\text{PrCoO}_3$  (JCPDS Card No. 25-1069) appears at 33.4°. In addition, the doubling feature of the unit cell is confirmed by the existence of a (001) peak, clearly observed at 11.4°. These results indicate the existence of both double perovskite and simple perovskite phases in SPN-A-PBC. The morphology of the SPN-A-PBC electrode is observed by SEM. As shown in Fig. 1c and d, the A-PBC particles are decorated with some nanorods. In contrast, the A-PBC precursor (PBC-1) only consists of many irregular particles with a size of approximate 0.5–1.5 μm (Fig. S3). This implies the establishment of a new composite after depositing the electrode, which is further confirmed by following TEM analysis. In addition, SEM images of the single A-PBC electrode are depicted in Fig. 1e and f for comparison.

The detailed phase and structural information of SPN-A-PBC were characterized by TEM. Fig. 2a and b show representative TEM images of

the SPN-A-PBC sample peeled off from the CGO substrate. It can be clearly seen that the SPNs with a diameter of 30–50 nm and a length of 100–200 nm are tightly anchored on the surface of the A-PBC particles, suggesting a surface-to-surface interfacial contact between A-PBC and SPN. To distinguish these two different composites, HRTEM images and SAED patterns are taken from different regions related to A-PBC and SPN. From HRTEM image of A-PBC (Fig. 2c), the contrast differences reveal a two-fold modulation of crystal structure along the  $[001]_p$  direction. The lattice spacing of 0.394 nm corresponds to the (100) facets of layered-type double perovskite  $\text{PrBaCo}_2\text{O}_{5.68}$  (JCPDS Card No. 53-0131). Fig. 2d shows the SAED pattern along the  $[100]_p$  zone axis of an A-PBC crystal. In addition to the strong Bragg diffractions of tetragonal perovskite structure, the extra superlattice diffractions at  $G_p \pm 1/2(001)_p^*$  associated with layered ordering arrangement of Pr and Ba along the  $[001]_p$  direction are observed. The HRTEM image of an individual SPN is displayed in Fig. 2e. The lattice fringes with a lattice distance of 0.278 nm are ascribed to the (220) facets of cubic simple perovskite  $\text{PrCoO}_3$  (JCPDS Card No. 25-1069). The corresponding SAED pattern (Fig. 2f) of a single SPN can be indexed on a primitive cubic perovskite structure along the  $[1\bar{1}0]_p$  zone axis, suggesting a  $[001]_p$  growth direction of SPN.

To further determine the composition of SPNs, HRTEM and SAED along different orientations and EDX spectra are performed on the SPN-A-PBC sample. Fig. 3a–f show three key SAED patterns along the  $[010]_p$ ,  $[1\bar{1}0]_p$  and  $[1\bar{1}1]_p$  zone axes and corresponding HRTEM images of an individual SPN. The strong reflections can be indexed on the cubic simple perovskite phase and no extra reflections for the cation ordering along the *c*-lattice parameter are observed. The SAED patterns and HRTEM images taken along different zone axes confirm the single-crystalline nature of SPNs. Furthermore, the HAADF-STEM images of the SPN-A-PBC sample also support the successful exsolution of SPNs from the A-PBC host lattice (Fig. 3g and i), which is further evidenced by STEM-EDX elemental mapping images and line-scanning profile. As specially shown in Fig. 3h, EDX mapping images indicate that all of the expected component elements (Pr, Ba, Co and O) are homogeneously and evenly distributed throughout the as-prepared SPN-A-PBC themselves. The line-scanning profile (Fig. 3j), with data taken at 0.5 nm intervals along a given 70 nm distance, shows the similar and consistent intensity for these elements spatially dispersed along a representative length of an individual nanorod.

### 3.2. Growth mechanism of the SPN-A-PBC electrocatalyst

In this study, the SPN-A-PBC electrode was fabricated after the depositing treatment (950 °C for 6 h in air) on a CGO substrate. More than likely, the *in situ* exsolving mechanism of SPNs seems to differ from those in the previous publications [25,31,32]. As usual, the certain cations are incorporated in the host lattice during the synthesis process under oxidizing condition, and subsequently a metallic or oxide catalyst exsolves as nanoparticles in reducing atmosphere. Nevertheless, in the case of SPN-A-PBC, the exsolution of SPNs from the A-PBC host lattice is achieved in ambient air. One might suppose that the depositing treatment plays a key role in the interfacial exsolution of SPNs. To elucidate this point, the different stages in fabricating the SPN-A-PBC electrode were examined by SEM and TEM. The A-PBC precursor (PBC-1) is composed of many irregular micronscale particles (Fig. 4a). Fig. 4b–e show the HRTEM images and corresponding FTT patterns taken from different regions in A-PBC. Besides double perovskite phase, cubic simple perovskite phase is also recognized on the surface of the A-PBC crystal. After depositing treatment (950 °C for 3 h), the A-PBC particles maintain their initial morphology, in which notably some nanoparticles exsolve on the surface of A-PBC and begin to grow into the rod-like shape (Fig. 4f). As prolonging the depositing time (6 h), a morphological transformation from nanoparticle to nanorod is finished completely, and the heterostructured SPN-A-PBC electrode is formed (Fig. 4g).

The roles of organic agents (terpineol and ethyl cellulose) and CGO substrate on the morphological evolution of A-PBC are also investigated. Two controlled experiments are carried out and the results are shown in Fig. S4. Firstly, the PBC-1 in. is directly calcined at 950 °C for 6 h in air, but without CGO electrolyte substrate. SEM image (Fig. S4a) shows that the SPNs exsolve from the A-PBC host, indicating that the CGO substrate has no obvious effect on the growth of SPNs. Secondly, the PBC-1 power is deposited on a CGO substrate at 950 °C for 6 h in air, but without terpineol and ethyl cellulose. As shown in Fig. S4b, the nanoparticles with a size of 50–100 nm are formed on the surface of the A-PBC particles. On the basis of above observations, one can speculate about an exsolving mechanism that results in the growth of SPNs. The exsolution of simple perovskite may mainly result from the inherent feature of double perovskite A-PBC. The A-PBC crystal is thermodynamically unstable due to A-site cation-deficiency. Consequently, B-site atoms have a strong exsolving force to grow outward from the host lattice [32]. On the other hand, we can assume that the A-site cation disordering occurs due to Ba-deficiency, further giving rise to the formation of simple perovskite phase in A-PBC. Thus, there is phase segregation on the surface of A-PBC during the subsequent calcining process. The observed SPN generation then is the result of a delicate balance between the high interface energy of double perovskite and simple perovskite. This leaves the simple perovskite phase no other choice to grow outward to minimize the energy. The morphology of the resulting simple perovskite is subsequently steered by the surface diffusion mechanism [38,39]. The similar exsolving phenomenon has been reported on the SrO nanorod-decorated simple perovskite  $\text{La}_{0.6}\text{Sr}_{0.4}\text{FeO}_{3-\delta}$ , prepared by *in situ* exsolving process in hydrogen and subsequent pure oxygen atmospheres [38]. It is concluded that the surface diffusion is dominating for the growth of rod-like SrO, and the effective transport species might be related to a hydroxylated  $\text{Sr}(\text{OH})_x$  specie. In the case of SPN-A-PBC, if the cation diffusion is controlled throughout the surface, a large density of nuclei is generated, finally merging to a dense layer of simple perovskite. Owing to abundant functional groups ( $-\text{OH}$ ,  $-\text{CN}$  and  $-\text{O}_2\text{N}$ ), the effective transport species ( $\text{M}-\text{OH}$ ,  $\text{M}-\text{CN}$  and  $\text{M}-\text{O}_2\text{N}$ ) can produce thank to the addition of terpineol and ethyl cellulose solvents. Upon the transport of these species to the SPN nuclei, they likely decompose under the heating-treatment condition and finally lead to the growth of SPNs, namely so-called “extrusion filaments”. In addition, the previous research proved that some functional groups have a destructive effect on the face-shaping process toward the simple perovskite oxides [40]. The rough nuclei grow longer along the special axis zone direction, and finally become a rod-like or pyramid shape. Without terpineol and ethyl cellulose, the cation bulk diffusion becomes more difficult, and the conical-shaped nanoparticles are obtained as evidenced by Fig. S4b. According to these results, we can demonstrate the positive effect the solvents in the exsolving process.

For comparison, the A-PBC (PBC-2) has also been synthesized at 1000 °C for 12 h in air. With combination of XRD and TEM analyses (Fig. S5), it is found that more simple perovskites are formed in A-PBC, relative to the SPN-A-PBC sample. After depositing the PBC-2 powder on a CGO substrate (950 °C for 6 h), only the micronscale particles are observed in the A-PBC electrode, as evidenced by SEM images (Fig. 1e and f). When the synthesis temperature is further reduced to 950 °C, a pure cubic simple perovskite phase ( $\text{Pr}_{0.5}\text{Ba}_{0.47}\text{CoO}_{3-\delta}$ ) can be identified in the product (Fig. S6). These results strongly imply that the simple perovskite phase prefers to be crystallized at reduced temperatures. As decreasing the synthesis temperature, more and more simple perovskites are formed. This weakens the difference of interface energy between double perovskite and simple perovskite, accounting for the resulting particles in the A-PBC electrode without any exsolving composites. A possible exsolving mechanism is proposed and schematically illustrated in Fig. 4h. At the suitable synthesis temperature (1050 °C), the phase segregation occurs on the surface region of A-PBC. Both layered-type double perovskite and simple perovskite exists in the PBC-

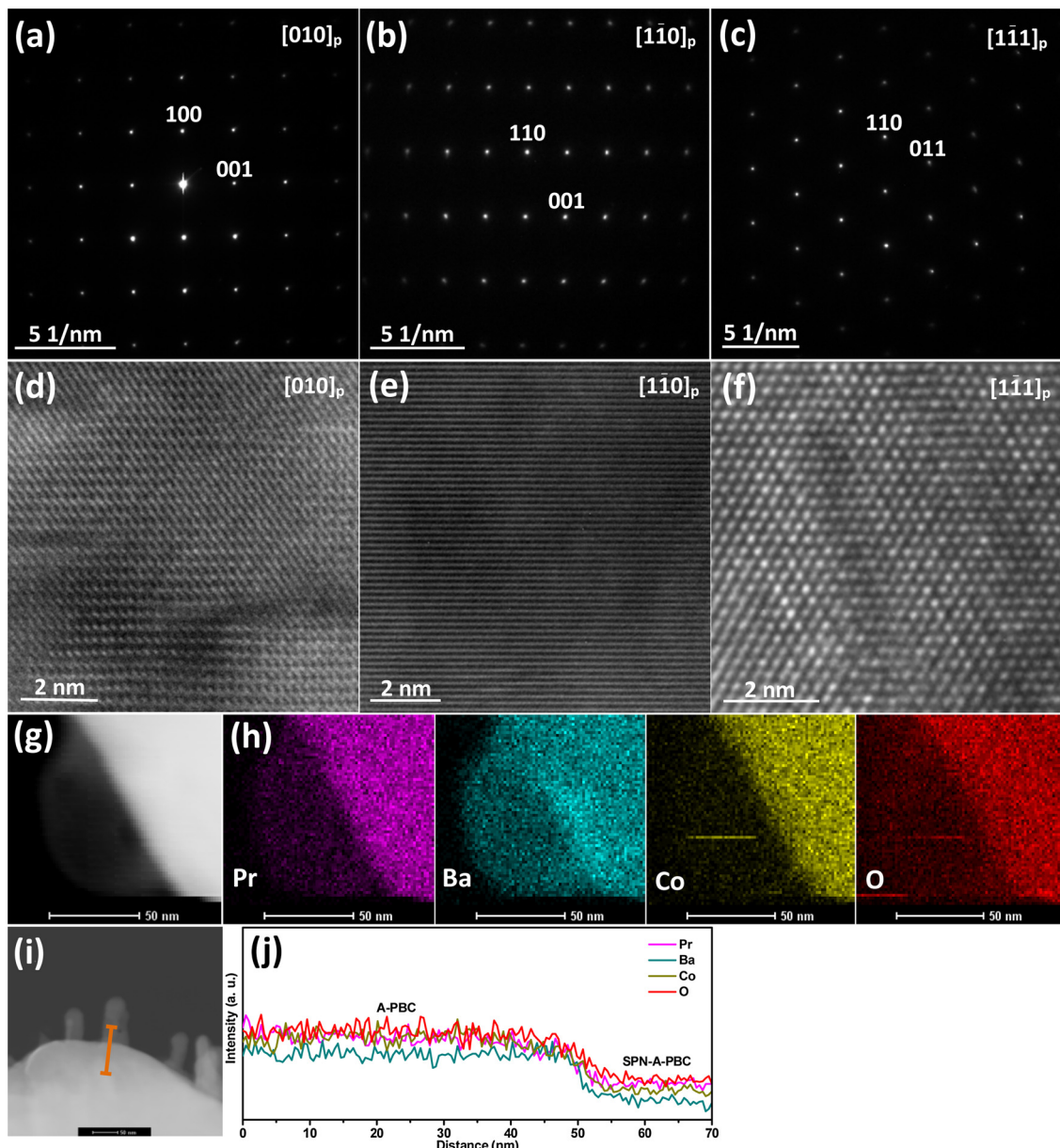


**Fig. 3.** (a, b and c) SAED patterns and corresponding (d, e and f) HRTEM images of an individual SPN along the [010]<sub>p</sub>, [1-10]<sub>p</sub> and [1-11]<sub>p</sub> zone axis. (g) HAADF-STEM image and corresponding (h) EDX mapping images of the SPN-A-PBC sample. (i) HAADF-STEM image and corresponding (j) EDX line-scanning profiles of the SPN-A-PBC sample.

1 sample. During the process of depositing the electrode (950 °C), the simple perovskite nanoparticles exsolve and gradually grow into the nanorods, in order to effectively minimize the interface energy.

### 3.3. Catalytic ORR activity, stability and CO<sub>2</sub>-durability of the SPN-A-PBC electrocatalyst

EIS was firstly used to assess the ORR activity of the hetero-structured SPN-A-PBC electrode on the symmetric half-cell with a configuration of SPN-A-PBC | CGO | SPN-A-PBC. Typical Nyquist plots of impedance spectra of the cell measured at 600–700 °C in air are shown in Fig. 5a, together with those of the A-PBC electrode for direct comparison. The difference between high-frequency and low-frequency intercepts of the impedance arc is defined as the polarization resistance ( $R_p$ ), including each ORR step, and so a lower  $R_p$  value means a higher catalytic ORR activity. Note that the ohmic resistance of the cell, mainly from the contribution of CGO electrolyte, has been subtracted from the

impedance spectra. As expected, the SPN-A-PBC electrode exhibits much improved ORR activity than that of the A-PBC electrode. For example, the  $R_p$  value of the A-PBC electrode is 0.10  $\Omega$  cm<sup>2</sup> at 700 °C, while the corresponding one is as low as 0.026  $\Omega$  cm<sup>2</sup> for the SPN-A-PBC electrode, approximately 74.0% lower. More detailed information is analyzed from EIS data to explore the ORR kinetics of the SPN-A-PBC electrode. The impedance spectra can be well fitted with an equivalent circuit of  $R_{\text{ohm}}\text{-}(R_{\text{HF}}\text{//}CPE_{\text{HF}})\text{-}(R_{\text{MF}}\text{//}CPE_{\text{MF}})\text{-}(R_{\text{LF}}\text{//}CPE_{\text{LF}})$ , where  $R_{\text{ohm}}$  is the ohmic resistance arising from the electrolyte, electrode, measuring device and wires;  $R_{\text{HF}}$ ,  $R_{\text{MF}}$ , and  $R_{\text{LF}}$  are the polarization resistances at high, medium and low-frequency, respectively;  $CPE_{\text{HF}}$ ,  $CPE_{\text{MF}}$  and  $CPE_{\text{LF}}$  represent the constant phase elements. As we know, the high and medium-frequency resistances ( $R_{\text{HF}}$  and  $R_{\text{MF}}$ ) are usually assigned to the oxygen ion and electron transfer reactions at the electrode, electrolyte, and collector/electrode interface; and the low-frequency one ( $R_{\text{LF}}$ ) reflects the oxygen surface process, involving the adsorption-desorption of molecular oxygen, the oxygen dissociation at

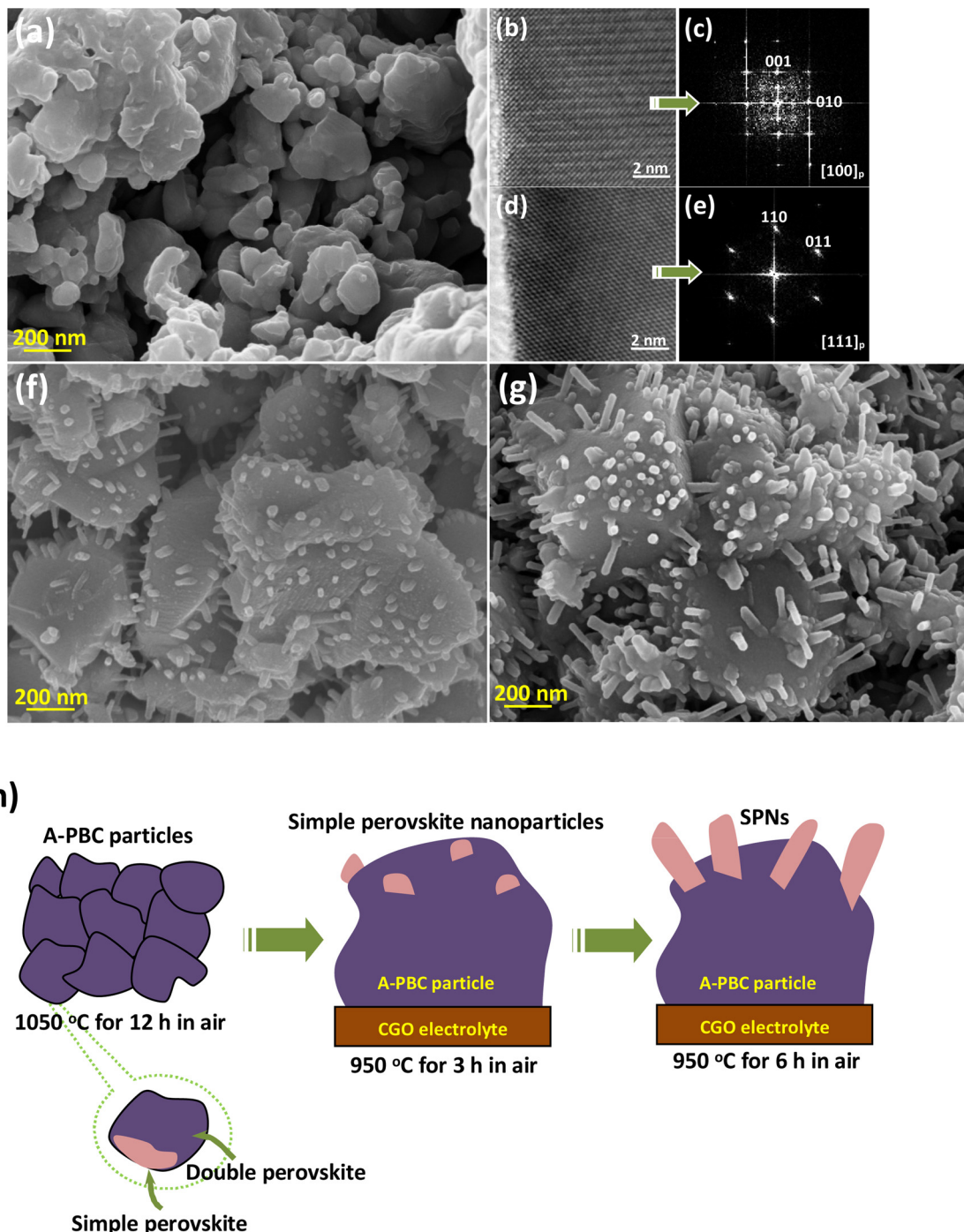


**Fig. 4.** (a) SEM image of the A-PBC (PBC-1) sample. (b, d) HRTEM images and corresponding (c, e) FFT patterns taken from different regions of the A-PBC sample. Surface-section view of SEM images of the SPN-A-PBC electrode deposited on a CGO substrate at 950 °C for (f) 3 h and (g) 6 h in air. (h) Schematic illustration of a possible exsolving mechanism of the SPN-A-PBC electrode.

the gas-electrode interface, and the surface diffusion of intermediate oxygen species etc [11,41,42]. At reduced temperatures, the low-frequency contribution in the impedance profiles increases evidently, indicating that the temperature mainly limits the oxygen surface process. The capacitance ( $C_i$ ), which is an independent parameter of the sample geometric characteristics and is a very useful tool to investigate the oxygen reduction process, can be calculated by the following equation [11]:

$$C_i = \frac{(R_i Q_i)^{1/n_i}}{R_i} \quad (1)$$

The detailed fitting parameters of impedance spectra for the A-PBC and SPN-A-PBC electrodes as a function of temperature are summarized in Table S1. It can be seen that the  $C_{HF}$  values for high-frequency arc are approximately  $10^{-5} \text{ F cm}^{-2}$ , which is attributed to the oxygen ion transport through the electrode/electrolyte interface [11]. Considering the  $C_{MF}$  values ( $\sim 10^{-3} \text{ F cm}^{-2}$ ), one can say that the medium-frequency arc may originate from the charge transfer reaction occurring on the electrode/gas interface [11,43]. In the case of  $C_{LF}$ , they fall within the range of  $\sim 10^{-1} \text{ F cm}^{-2}$ , probably due to the dissociation of absorbed molecular oxygen in the electrode materials [43].

The  $R_{HF}$ ,  $R_{MF}$  and  $R_{LF}$  values of the A-PBC and SPN-A-PBC electrodes

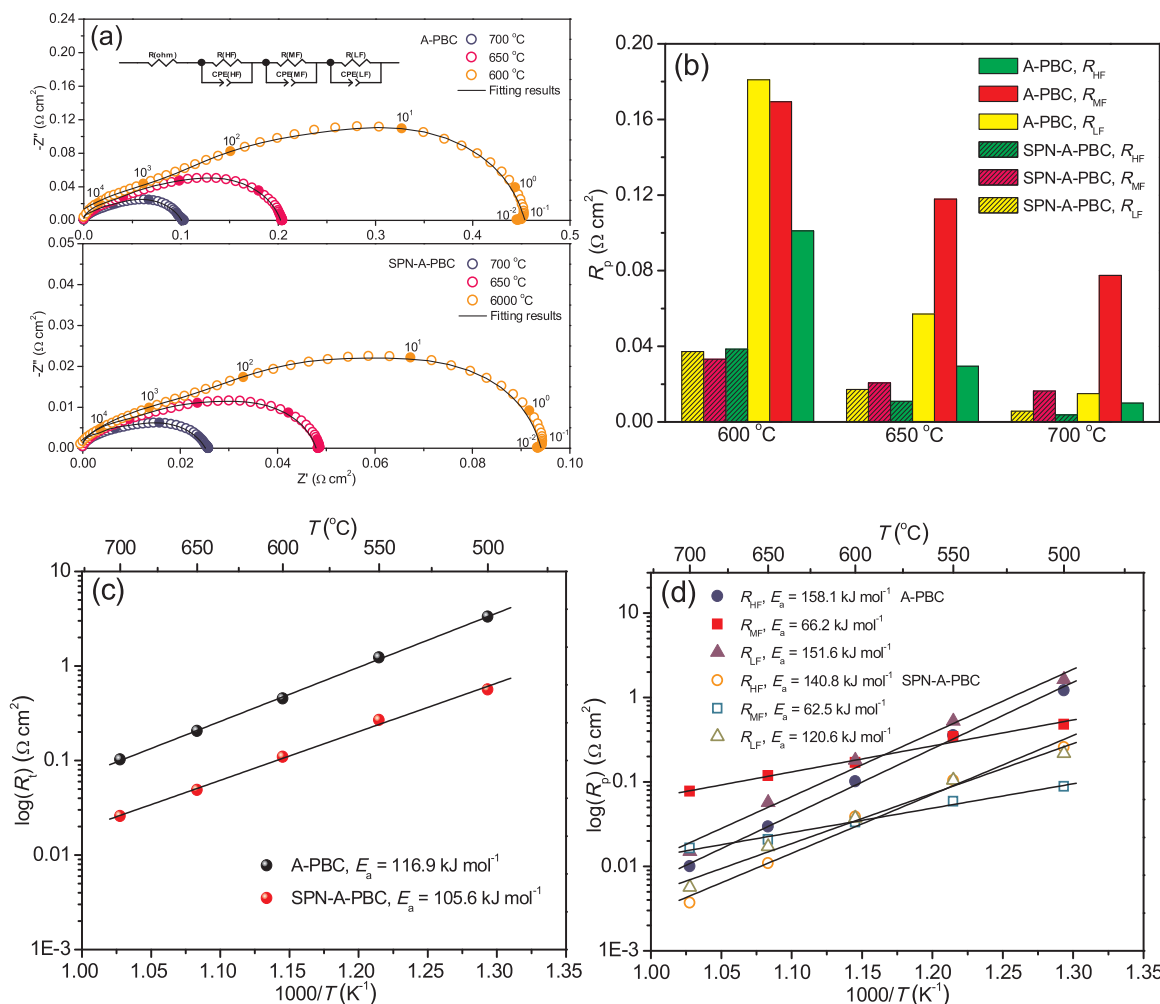


**Fig. 5.** (a) Typical Nyquist plots of impedance spectra of the symmetric half-cells with the A-PBC and SPN-A-PBC electrodes at 600–700 °C in air (the numbers indicate the measuring frequency). The corresponding equivalent circuit is also shown as inset. (b) Comparison of  $R_{HF}$ ,  $R_{MF}$  and  $R_{LF}$  for the A-PBC and SPN-A-PBC electrodes between 600 and 700 °C. Arrhenius plots of (c)  $R_t$ , (d)  $R_{HF}$ ,  $R_{MF}$  and  $R_{LF}$  for the A-PBC and SPN-A-PBC electrodes between 500 and 700 °C.

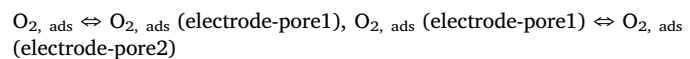
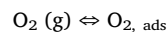
at 600–700 °C are shown in Fig. 5b. As compared with the A-PBC electrode, both of  $R_{HF}$ ,  $R_{MF}$  and  $R_{LF}$  of the SPN-A-PBC electrode decrease greatly. The Arrhenius plots of total polarization resistance ( $R_t$ ),  $R_{HF}$ ,  $R_{MF}$  and  $R_{LF}$  for the A-PBC and SPN-A-PBC electrodes between 500 and 700 °C are shown in Fig. 5c and d. Here is the fact that the SPN-A-PBC electrode meets the requirement of ideal  $R_p$  of IT-SOFC component ( $0.1 \Omega \text{ cm}^2$  [3]). Even at 500 °C, a low  $R_p$  value reaches as low as  $0.56 \Omega \text{ cm}^2$ . Based on the slopes of these plots, the activation energies associated with different electrochemical processes described by  $R_t$ ,  $R_{HF}$ ,  $R_{MF}$  and  $R_{LF}$  are calculated and listed in Fig. 5c and d. The overall activation barrier ( $105.6 \text{ kJ mol}^{-1}$ ) for ORR of SPN-A-PBC is lower than that of A-PBC ( $116.9 \text{ kJ mol}^{-1}$ ) (Fig. 5c), indicating that the electrocatalytic ORR kinetics may be accelerated on the SPN-A-PBC electrode. Most importantly, it is noteworthy that the activation energy related to  $R_{LF}$  decreases significantly (Fig. 5d). This verifies that the exsolved SPNs effectively improve the oxygen surface exchange process.

The SPN-A-PBC electrode also exhibits an excellent long-term stability, and the variation of  $R_p$  as a function of time at 700 °C in air is shown in Fig. S7a. As can be clearly seen, the  $R_p$  value almost keeps a constant over the measuring period, with a negligible degradation rate (only  $8.3 \mu\Omega \text{ cm}^2 \text{ h}^{-1}$ ). According to the research on the perovskite electrodes [44,45], the performance degradation may be attributed to the change of the electrode surface composition, such as phase segregation or transformation, and grain coarsening, particularly at grain boundaries. Indeed, SEM image (Fig. S7b) shows that after long-term

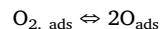
stability measurements there is no obvious change in the microstructure of the SPN-A-PBC electrode. It is concluded that the exsolved SPNs may inhibit the surface phase segregation and grain coarsening, leading to the stable SPN-A-PBC air electrode.

The ORR kinetics of the SPN-A-PBC electrode is further studied by measuring the impedance spectra at various oxygen partial pressures at 700 °C, as shown in Fig. 6a. The correlation between the electrode polarization resistance and  $pO_2$  can be expressed as  $R_p = k(pO_2)^{-n}$ , where  $k$  is a constant, and the different exponential  $n$  is experimentally found to characterize the nature of ORR steps occurring on the electrode. The following relationships between the  $n$  values and the electrochemical steps in ORR have been reported [11,46].

When  $n = 1$ , the step involves the adsorption and diffusion of molecular oxygen:



When  $n = 1/2$ , the step involves the dissociation of adsorbed molecular oxygen to atomic oxygen:



When  $n = 1/4$ , the step involves the charge transfer/oxygen vacancy healing reaction:

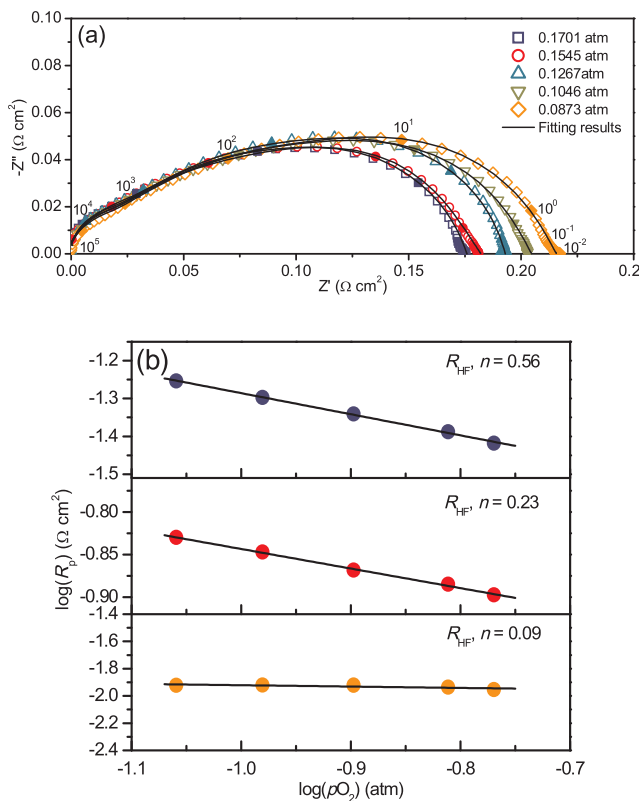
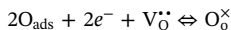


**Fig. 6.** (a) Nyquist plots of Impedance spectra for the SPN-A-PBC electrode at various oxygen partial pressures at 700 °C (the numbers indicate the measuring frequency). (b) The correlation between  $R_{HF}$ ,  $R_{MF}$ ,  $R_{LF}$  and  $pO_2$  of the SPN-A-PBC electrode at 700 °C.



When  $n = 0$ , the step involves the oxygen transport through the electrode/electrolyte interface



Fig. 6b shows the correlation between  $R_{HF}$ ,  $R_{MF}$ ,  $R_{LF}$  and  $pO_2$  of the SPN-A-PBC electrode at 700 °C, in terms of the linear dependence between the logarithm of  $R_p$  and the logarithm of  $pO_2$ . The  $R_{HF}$ ,  $R_{MF}$  and  $R_{LF}$  increase with decreasing the oxygen partial pressure. From the slopes of the fitting results in Fig. 6b, the  $n$  values for the high, medium and low-frequency contributions are 0.09, 0.23 and 0.56, close to 0, 1/4 and 1/2, respectively. Hence the rate-limiting steps for ORR on the SPN-A-PBC electrode are determined to be the oxygen ion transport through the electrode/electrolyte interface, charge transfer/oxygen vacancy healing reaction at the electrode/gas interface, and the dissociation of adsorbed molecular oxygen. This is consistent with the impedance tests as a function of temperature in air.

In addition to high electro-catalytic activity toward ORR, an important concern for the alkaline earth-containing perovskites is their durability, which limits their commercialization in SOFCs. The Ba/Sr-rich perovskites normally have a poor stability when exposed to contaminants customarily encountered in ambient air, such as  $CO_2$ , forming the  $BaCO_3/SrCO_3$  phase because of more basic surfaces in oxides easily poisoned by  $CO_2$  [13,47]. Fig. 7 shows the variation of  $R_p$  of the SPN-A-PBC electrode in air with different concentrations of  $CO_2$  (0, 1, 4, 6 and 10 vol %) as a function of time at 700 °C. It can be seen that the  $R_p$  increases slowly with increasing the concentration of  $CO_2$ . In particular, the  $R_p$  values nearly remain unchanged as a function of time at a constant concentration of  $CO_2$ . After introducing different concentrations of  $CO_2$  (0, 1, 4, 6 and 10 vol %) into air, the average  $R_p$  values are 0.024, 0.040, 0.055, 0.078 and 0.120  $\Omega cm^2$ , respectively.

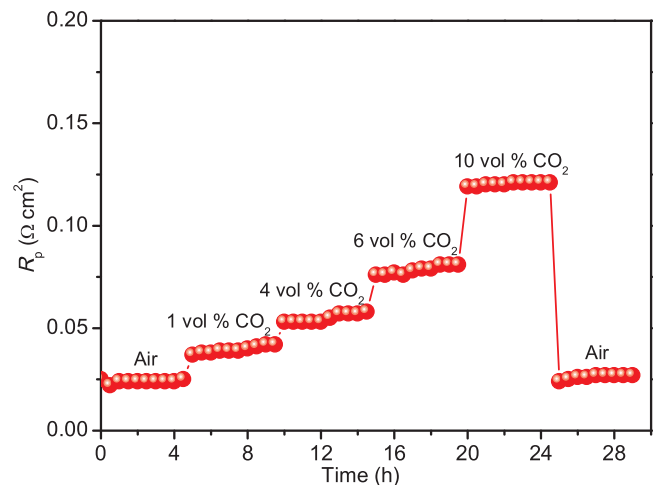


**Fig. 7.** Variation of  $R_p$  of the SPN-A-PBC electrode in air with different  $CO_2$  concentrations as a function of time at 700 °C.

When the  $CO_2$  atmosphere is then removed, a stable  $R_p$  value of ~0.027  $\Omega cm^2$  is recovered over a period of 4 h. These  $R_p$  values still satisfy the cathode application in the intermediate temperature range. Table S2 lists the  $R_p$  values of the SPN-A-PBC and classical/state-of-art electrodes in different concentrations of  $CO_2$  [36, S1-S3]. The  $R_p$  value of the SPN-A-PBC electrode is 0.12  $\Omega cm^2$  after introducing 10 vol %  $CO_2$  at 700 °C. The degradation of the classical perovskite electrodes is more serious; e.g. the  $R_p$  value of BSCF reaches 4.81  $\Omega cm^2$  in 10 vol %  $CO_2$  at 600 °C [S1]. The  $CO_2$ -durability measurements for the SPN-A-PBC electrode demonstrate its excellent tolerance to  $CO_2$ , promising its practical use in a portable single chamber SOFC.

#### 3.4. Electrochemical performance of the single cell with the SPN-A-PBC cathode

To test the performance of the A-PBC and SPN-A-PBC cathodes in a complete single cell, the anode-supported fuel cells are fabricated using a Ni/YSZ anode support (~300  $\mu m$  thick), an YSZ electrolyte (~8  $\mu m$  thick), a CGO thin film buffer layer (~5  $\mu m$  thick) and the A-PBC (SPN-A-PBC) cathode (~20  $\mu m$  thick). Cross-section view of SEM images of the cell components is depicted in Fig. 8a and b. For both of the A-PBC and SPN-A-PBC-based cells, YSZ electrolyte component is very dense, ensuring the high open-circuit voltages of the single cells at operating temperatures. The porous cathode attaches greatly to the CGO buffer layer without obvious interfacial delamination, which offers a facile gas-phase diffusion pathway and suggests a thermal compatibility between the cathode and the CGO buffer layer. Fig. 8c and d show the  $V-I$  and  $P-I$  curves of the single cells with the A-PBC and SPN-A-PBC cathodes at 600–700 °C, using humidified  $H_2$  (97%  $H_2$ /3%  $H_2O$ ) and ambient air as the fuel and the oxidant, respectively. The open circuit voltage (OCV) values are close to Nernst potentials, suggesting a good sealing of the cells and a gas-tight characteristic of the electrolyte component. At 700 °C, the maximum power density is 1.1  $W cm^{-2}$  for the SPN-A-PBC cathode-based single cell, which is much higher than that of the single cell with the A-PBC cathode (0.62  $W cm^{-2}$ ) and can be comparable to the performance ever reported (Table S3) [S3-S12]. These results confirm a highly electro-catalytic activity for ORR of the SPN-A-PBC cathode under realistic operating conditions. The impedance spectra of the single cells deliver the similar ohmic resistances mainly originating from the electrolyte component (Fig. S8). For instance, the ohmic resistances are 0.17 and 0.16  $\Omega cm^2$  for the A-PBC and SPN-A-PBC-based cells at 700 °C, respectively. Assuming that the resistance of the anode/electrolyte/buffer layer is nearly same for both cells, since they are fabricated in the same procedure and batch, the improved cathode performance of SPN-A-PBC is reasonably responsible

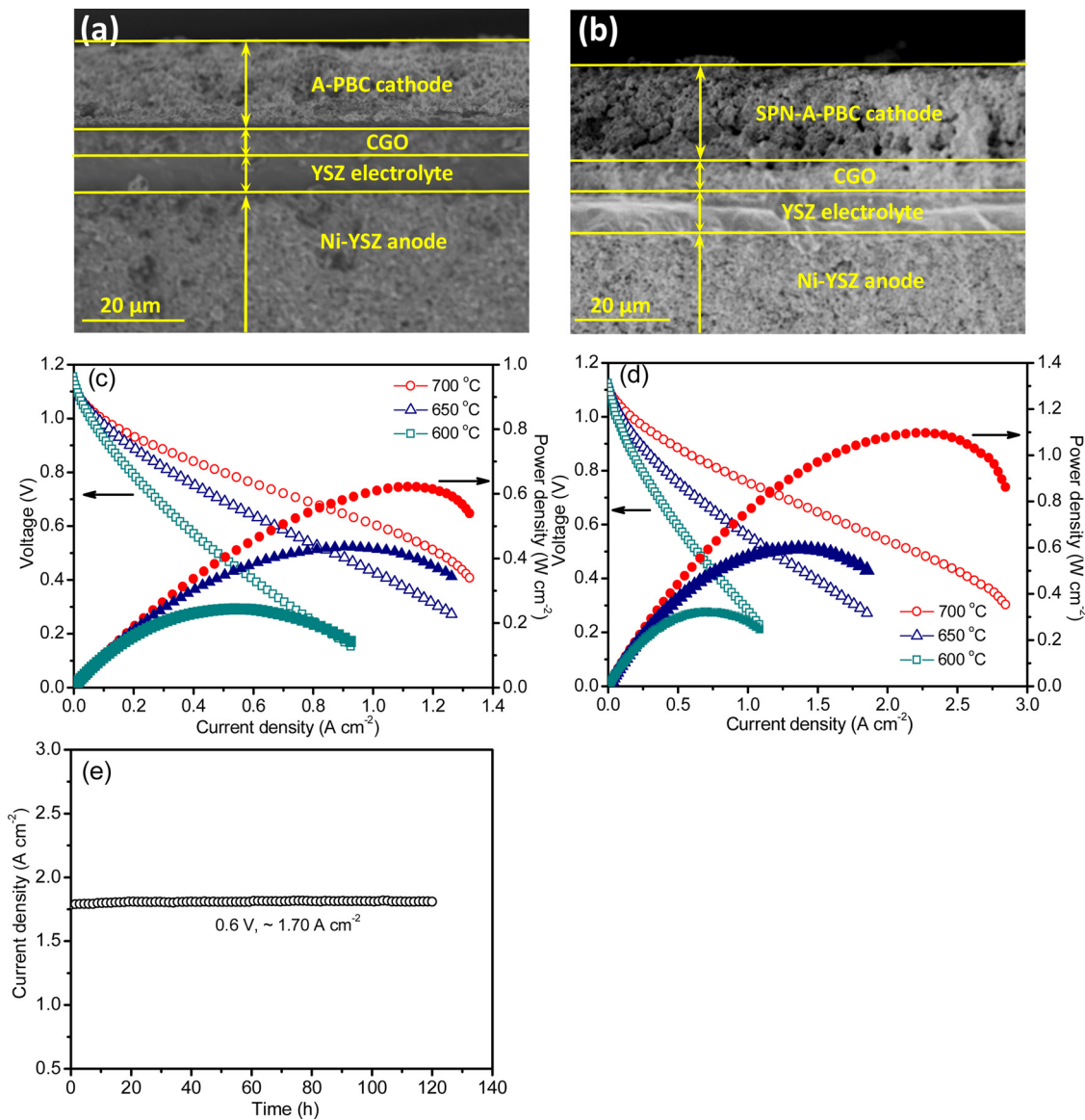


**Fig. 8.** Cross-section view of SEM images of the anode-supported single cells with a Ni-YSZ anode, an YSZ electrolyte, a CGO buffer layer and the (a) A-PBC and (b) SPN-A-PBC cathodes. The  $V$ - $I$  and  $P$ - $I$  curves of the single cells with the (c) A-PBC and (d) SPN-A-PBC cathodes at 600–700 °C. (e) Long-term stability test of a single cell with the SPN-A-PBC cathode at a constant loading voltage of 0.6 V at 700 °C for 120 h.

for the enhanced power output. As expected, the lower overall polarization resistance is obtained in the cell with the SPN-A-PBC cathode, e.g. 0.30 and 0.14  $\Omega$  cm<sup>2</sup> for the A-PBC and SPN-A-PBC-based cells, respectively.

To check the long-term stability of the SPN-A-PBC cathode, the single cell is measured under a constant loading condition (0.6 V) at 700 °C for 120 h. As can be seen (Fig. 8e), the fuel cell shows a highly stable power output (~1.70 A cm<sup>-2</sup>), which agrees well with the  $R_p$  tests over a same period. Although IT-SOFCs with the higher power densities have been reported so far as listed in Table S3, it is still believed that the SPN-A-PBC cathode-based fuel cell is one of the most available IT-SOFCs, combined with high power density and superior long-term stability.

### 3.5. Effects on the catalytic ORR activity of the SPN-A-PBC electrocatalyst

To study the effects on the catalytic ORR activity of the SPN-A-PBC electrocatalyst, the A-PBC (PBC-1) and SPN-A-PBC electrocatalysts were examined by  $O_2$ -TPD measurements. The great redox property of cobalt ions and the oxygen mobility in SPN-A-PBC were confirmed by

the  $O_2$ -TPD evidence. With the programmed increase in temperature, the cobalt ions undergo a thermal reduction process, accompanied with the release of species oxygen. Fig. 9a shows the  $O_2$ -TPD profiles of the A-PBC and SPN-A-PBC electrocatalysts. There are four series of desorption peaks observed in all of two profiles. The first small peak (O1) between 40 and 160 °C is ascribed to physically adsorbed species  $O_2$  weakly bound to the surface [48,49], which is easily desorbed in low temperature range. The second broad one over the temperature range of ~240–500 °C is usually referred as  $\alpha_1$ - $O_2$  (O2), associated with the desorption of chemically adsorbed species  $O_2^-$  (and/or O) generated by the adsorbed  $O_2$  on the surface anion vacancies [50]. The subsequently broad one located at 510–680 °C describes the  $\alpha_2$ - $O_2$  (O3) desorption behavior. The reduction of unstable  $Co^{4+}$  to  $Co^{3+}$  with  $O_2$  desorption and vacancy formation occurs on the surface domain, while the lattice oxygen in the bulk diffuses from the bulk to the surface via the oxygen vacancy defects [51]. At high temperature, a sharp  $\beta$ - $O_2$  (O4) desorption reduction at about 825 °C can be observed, corresponding to a further reduction of  $Co^{3+}$  to  $Co^{2+}$  [50]. We assume that the  $Pr^{3+}$  and  $Ba^{2+}$  ions maintain their oxidation states because they are more difficult to be reduced than cobalt ions. In A-PBC and SPN-A-PBC, the cobalt

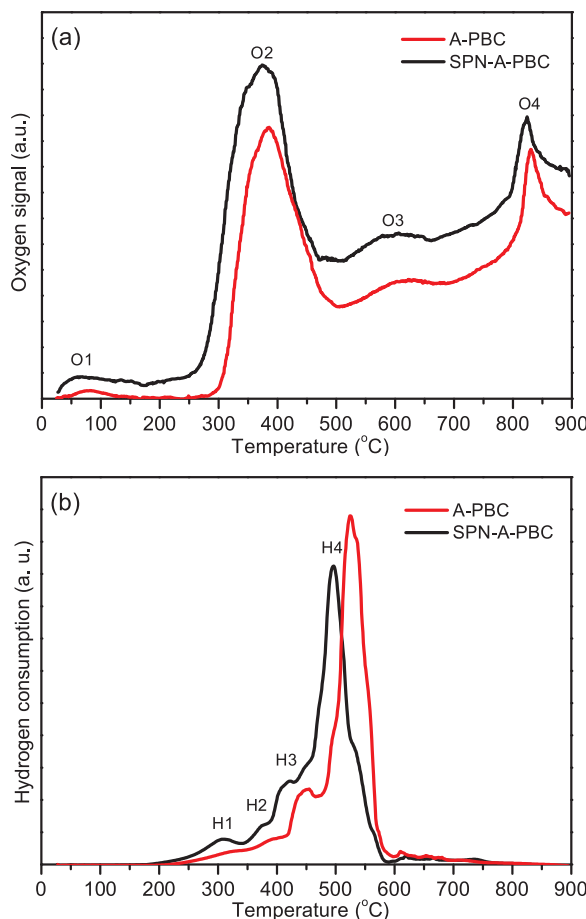


**Fig. 9.** (a) The  $O_2$ -TPD and (b)  $H_2$ -TPR profiles of the A-PBC and SPN-A-PBC electrocatalysts.

ions are emphasized to account for nearly 100% reduction related with the desorbed  $\alpha_2$  and  $\beta$  oxygen. The details of the oxygen desorption peaks are summarized in Table 1. The onset temperature for releasing oxygen is an important feature to estimate the level of the oxidation-state change of cobalt ions in an oxide. Compared to those of A-PBC, both  $\alpha$ - and  $\beta$ - $O_2$  peaks of SPN-A-PBC shift to lower temperatures and the peak areas increase. These reveal that the exsolved SPNs not only improves the  $\alpha$ - $O_2$  desorption due to an increase in surface oxygen vacancies but also enhances the mobility of lattice  $O_2$ . As can be seen, HRTEM image of A-PBC (PBC-1) shows a perfect lattice from the surface to the bulk (Fig. S9a), but a disordered atomic arrangement is observed at the SPN/A-PBC interface in the SPN-A-PBC sample (Fig. S9b). This indicates that more surface oxygen vacancies may be formed at the SPN/A-PBC interface. The corresponding intensity line-profile at the SPN/A-PBC interface is shown in Fig. S9c. We think that the higher deviation of column intensity for anion columns is due to the distribution of oxygen vacancies in anion sites. XPS technique is also used to study the chemical environment of surface oxygen. The O 1s core-level spectra of the A-PBC (PBC-1) and SPN-A-PBC samples are shown in Fig. S10. All of two spectra can be deconvoluted in to three peaks located at  $\sim$ 528.1, 530.6 and 532.4 eV, respectively, in conformity with

the bonding between oxygen atoms and metals ( $O'$ ), defect sites with abundant low oxygen coordination ( $O''$ ), and hydroxyl groups of adsorbed water molecules on surface ( $O'''$ ) [S13–S15]. Notably, the intensity and area of  $O''$  peak for SPN-A-PBC is much higher than those of A-PBC, suggesting an increase in superficial oxygen vacancies, e. g. oxygen vacancy percentages of 49.3% and 57.5% for A-PBC and SPN-A-PBC, respectively. The larger amount of oxygen vacancies may favor the oxygen surface exchange process [S16].

In addition, it is noted that the amount of  $O_1$  is also promoted in SPN-A-PBC. The regular trend in change of the amount of  $O_1$  is related to the specific surface area, implying that the large specific surface area may account for the adsorption of physically adsorbed oxygen. This is consistent with an increase in BET surface area of SPN-A-PBC ( $4.85\text{ m}^2\text{ g}^{-1}$ ), higher than that of A-PBC (PBC-1) ( $2.70\text{ m}^2\text{ g}^{-1}$ ) (Fig. S11). When a mixed ionic-electronic conductor (MIEC) is chosen as the cathode, the whole electrode surface can supply active sites for ORR because of natural oxygen ion migration in the bulk, so the ORR zone is extended from triple phase boundary (TPB, electrode/gas/electrolyte) to two-phase boundary (2PB, electrode/gas) [42]. The ORR occurs not only at TPB but also at 2PB, and electrochemically active zone is the sum of TPB and 2PB sites. We can suppose that the exsolved SPNs may enhance the specific surface area and the length of 2PB and TPB, supplying more electro-catalytic active sites for ORR.

The excellent redox potential of cobalt ions in SPN-A-PBC was further confirmed by  $H_2$ -TPR results. As shown in Fig. 9b, on the  $H_2$ -TPR profile of A-PBC, three low-temperature reduction peaks (H1, H2 and H3) at 338, 386 and 454 °C can be assigned to the chemically adsorbed oxygen on the surface of the catalyst and the reduction of  $Co^{4+}/Co^{3+}$  to  $Co^{2+}$ . The reduction peak (H4) at 529 °C is due to the reduction of  $Co^{2+}$  to  $Co^0$  [52,53]. After the exsolution of SPNs, the onset temperatures of the reduction peaks become lower, in accordance with the results of  $O_2$ -TPD. It is proved that the cobalt ions with high valence state in SPN-A-PBC are easier to be reduced to a low valence state. The fitted peak area, peak center and  $H_2$  consumption are listed in Table 2. The easy transition in the oxidation state of the cobalt ions in SPN-A-PBC indicates an excellent redox property and enhanced mobility of lattice  $O_2$ , which is responsible for its highly catalytic ORR activity.

#### 4. Conclusion

In summary, the heterostructured simple perovskite nanorod-decorated A site-deficient double perovskite  $PrBa_{0.94}Co_2O_{5+\delta}$  (SPN-A-PBC) electrocatalyst, with the highly electro-catalytic ORR activity, the superior operating stability and the excellent  $CO_2$ -durability, has been prepared by *in situ* exsolving process and evaluated in both symmetric half-cell and single cell. The SPN-A-PBC electrode exhibits a polarization resistance as low as  $0.025\text{ }\Omega\text{ cm}^2$  at 700 °C. The anode-supported single cell with the SPN-A-PBC cathode delivers a maximum power density of  $1.1\text{ W cm}^{-2}$  at 700 °C. The improved redox property and oxygen mobility of SPN-A-PBC as confirmed by  $O_2$ -TPD and  $H_2$ -TPR, and tightly anchored SPNs on the A-PBC host favor the highly catalytic ORR activity. This heterostructured electrocatalyst would be applied in other chemical and energy transformation systems, and this design concept may open up a new strategy for constructing the heterostructured composite materials.

**Table 1**

The details of the oxygen desorption peaks for the A-PBC and SPN-A-PBC electrocatalysts based on  $O_2$ -TPD profiles.

Sample	$\alpha_1$ - $O_2$ Area (digits)	$\alpha_2$ - $O_2$ Area (digits)	$\beta$ - $O_2$ Area (digits)	$\alpha_1$ - $O_2$ Peak center (°C)	$\alpha_2$ - $O_2$ Peak center (°C)	$\beta$ - $O_2$ Peak center (°C)
A-PBC	505.6	896.8	518.6	385.6	630.0	830.4
SPN-A-PBC	662.8	1021.3	784.8	367.6	601.4	824.6

**Table 2**

The details of the hydrogen reduction peaks for the A-PBC and SPN-A-PBC electrocatalysts based on  $H_2$ -TPR profiles.

	A-PBC	SPN-A-PBC
H1 area (digits)	792.9	1189.1
H2 area (digits)	367.1	2009.9
H3 area (digits)	3892.1	2148.0
H4 area (digits)	13,805.1	13390.5
H1 peak center (°C)	338.3	309.7
H2 peak center (°C)	386.0	393.2
H3 peak center (°C)	453.8	428.4
H4 peak center (°C)	528.9	497.5
H1 consumption (mol g <sup>-1</sup> )	$3.09 \times 10^{-4}$	$4.63 \times 10^{-4}$
H2 consumption (mol g <sup>-1</sup> )	$1.43 \times 10^{-4}$	$7.82 \times 10^{-4}$
H3 consumption (mol g <sup>-1</sup> )	$1.52 \times 10^{-3}$	$8.36 \times 10^{-4}$
H4 consumption (mol g <sup>-1</sup> )	$5.37 \times 10^{-3}$	$5.21 \times 10^{-3}$

## Acknowledgements

This work was supported by National Natural Sciences Foundation of China (51372073), Research Foundation of Key Laboratory of Functional Inorganic Material Chemistry (Heilongjiang University), Open Foundation of State Key Laboratory of Rare Earth Resource Utilization, Changchun Institute of Applied Chemistry (RERU2018006), and Natural Science Foundation of Heilongjiang Province (E2016055 and 2013TD002).

## Appendix A. Supplementary data

Supplementary material related to this article can be found, in the online version, at doi:<https://doi.org/10.1016/j.apcatb.2019.02.056>.

## References

- D. Chen, C. Chen, Z.M. Baiyee, Z. Shao, F. Ciucci, Nonstoichiometric oxides as low-cost and highly-efficient oxygen reduction/evolution catalysts for low-temperature electrochemical devices, *Chem. Rev.* 115 (2015) 9869–9921.
- R.J. Gorte, S. Park, J.M. Vohs, Direct oxidation of hydrocarbons in a solid-oxide fuel cell, *Nature* 404 (2000) 265–267.
- B.C.H. Steele, A. Heinzel, Materials for fuel-cell technologies, *Nature* 414 (2001) 345–352.
- E.D. Wachsman, K.T. Lee, Lowering the temperature of solid oxide fuel cells, *Science* 334 (2011) 935–939.
- F.S. da Silva, T.M. de Souza, Novel materials for solid oxide fuel cell technologies: a literature review, *Int. J. Hydrogen Energy* 42 (2017) 26020–26036.
- L. Fan, B. Zhu, P.-C. Su, C. He, Nanomaterials and technologies for low temperature solid oxide fuel cells: recent advances, challenges and opportunities, *Nano Energy* 45 (2018) 148–176.
- B. Liu, X. Chen, Y. Dong, S.S. Mao, M. Cheng, A high-performance, nanostructured  $Ba_{0.5}Sr_{0.5}Co_{0.8}Fe_{0.2}O_{3-\delta}$  cathode for solid-oxide fuel cells, *Adv. Energy Mater.* 1 (2011) 343–346.
- Z. Shao, S.M. Haile, A high-performance cathode for the next generation of solid oxide fuel cells, *Nature* 431 (2004) 170–173.
- C.-Y. Yoo, J.H. Park, D.S. Yun, Y.A. Lee, K.S. Yun, J.H. Yoon, H. Yoon, J.H. Joo, J.H. Yu, Unraveling crystal structure and transport properties of fast ion conducting  $SrCo_{0.9}Nb_{0.1}O_{3-\delta}$ , *J. Phys. Chem. C* 120 (2016) 22248–22256.
- W.H. Kan, A.J. Samson, V. Thangadurai, Trends in electrode development for next generation solid oxide fuel cells, *J. Mater. Chem. A* 4 (2016) 17913–17932.
- J.S.A. Carneiro, R.A. Brocca, M.L.R.S. Lucena, E. Nikolla, Optimizing cathode materials for intermediate-temperature solid oxide fuel cells (SOFCs): oxygen reduction on nanostructured lanthanum nickelate oxides, *Appl. Catal. B Environ.* 200 (2017) 106–113.
- K. Efimov, Q. Xu, A. Feldhoff, Transmission electron microscopy study of  $Ba_{0.5}Sr_{0.5}Co_{0.8}Fe_{0.2}O_{3-\delta}$  perovskite decomposition at intermediate temperatures, *Chem. Mater.* 22 (2010) 5866–5875.
- Y. Zhu, J. Sunarso, W. Zhou, Z. Shao, Probing  $CO_2$  reaction mechanisms and effects on the  $SrNb_{0.1}Co_{0.9-x}Fe_xO_{3-\delta}$  cathodes for solid oxide fuel cells, *Appl. Catal. B Environ.* (2015) 172–173 52–57.
- Y. Chen, S. Yoo, X. Li, D. Ding, K. Pei, D. Chen, Y. Ding, B. Zhao, R. Murphy, B. de Glee, J. Liu, M. Liu, An effective strategy to enhancing tolerance to contaminants poisoning of solid oxide fuel cell cathodes, *Nano Energy* 47 (2018) 474–480.
- S.Y. Lai, D. Ding, M. Liu, M. Liu, F.M. Alamgir, Operando and in situ X-ray spectroscopies of degradation in  $La_{0.6}Sr_{0.4}Co_{0.2}Fe_{0.8}O_{3-\delta}$  thin film cathodes in fuel cells, *ChemSusChem* 7 (2014) 3078–3087.
- L. Zhang, S. Li, T. Xia, L. Sun, L. Huo, H. Zhao, Co-deficient  $PrBaCo_{2-x}O_{6-\delta}$  perovskites as cathode materials for intermediate-temperature solid oxide fuel cells: enhanced electrochemical performance and oxygen reduction kinetics, *Int. J. Hydrogen Energy* 43 (2018) 3761–3775.
- G. Kim, S. Wang, A.J. Jacobson, L. Reimus, P. Brodersen, C.A. Mims, Rapid oxygen ion diffusion and surface exchange kinetics in  $PrBaCo_2O_{5+x}$  with a perovskite related structure and ordered A cations, *J. Mater. Chem.* 17 (2007) 2500–2505.
- M. Burriel, J. Peña-Martínez, R.J. Chater, S. Fearn, A.V. Berenov, S.J. Skinner, J.A. Kilner, Anisotropic oxygen ion diffusion in layered  $PrBaCo_2O_{5+\delta}$ , *Chem. Mater.* 24 (2012) 613–621.
- I.D. Seymour, A. Chroneos, J.A. Kilner, R.W. Grimes, Defect processes in orthorhombic  $LnBaCo_2O_{5.5}$  double perovskites, *Phys. Chem. Chem. Phys.* 13 (2011) 15305–15310.
- R. Pelosato, G. Cordaro, D. Stucchi, C. Cristiani, G. Dotelli, Cobalt based layered perovskites as cathode material for intermediate temperature solid oxide fuel cells: a brief review, *J. Power Sources* 298 (2015) 46–67.
- C. Lim, A. Jun, H. Jo, K.M. Ok, J. Shin, Y.-W. Ju, G. Kim, Influence of Ca-doping in layered perovskite  $PrBaCo_2O_{5+\delta}$  on the phase transition and cathodic performance of a solid oxide fuel cell, *J. Mater. Chem. A* 4 (2016) 6479–6486.
- S. Park, S. Choi, J. Shin, G. Kim, A collaborative study of sintering and composite effects for a  $PrBa_{0.5}Sr_{0.5}Co_{1.5}Fe_{0.5}O_{5+\delta}$  IT-SOFC cathode, *RSC Adv.* 4 (2014) 1775–1781.
- Q. Zhou, F. Wang, Y. Shen, T. He, Performances of  $LnBaCo_2O_{5+x}Ce_{0.8}Sm_{0.2}O_{1.9}$  composite cathodes for intermediate-temperature solid oxide fuel cells, *J. Power Sources* 195 (2010) 2174–2181.
- L. dos Santos-Gómez, J.M. Porras-Vázquez, E.R. Losilla, D. Marrero-López, Improving the efficiency of layered perovskite cathodes by microstructural optimization, *J. Mater. Chem. A* 5 (2017) 7896–7904.
- Y. Zhu, W. Zhou, R. Ran, Y. Chen, Z. Shao, M. Liu, Promotion of oxygen reduction by exsolved silver nanoparticles on a perovskite scaffold for low-temperature solid oxide fuel cells, *Nano Lett.* 16 (2016) 512–518.
- M.E. Lynch, L. Yang, W. Qin, J.-J. Choi, M. Liu, K. Blinn, M. Liu, Enhancement of  $La_{0.6}Sr_{0.4}Co_{0.2}Fe_{0.8}O_{3-\delta}$  durability and surface electrocatalytic activity by  $La_{0.85}Sr_{0.15}MnO_3 \pm \delta$  investigated using a new test electrode platform, *Energy Environ. Sci.* 4 (2011) 2249–2258.
- E. Mutoro, E.J. Crumlin, M.D. Biegalski, H.M. Christen, Y. Shao-Horn, Enhanced oxygen reduction activity on surface-decorated perovskite thin films for solid oxide fuel cells, *Energy Environ. Sci.* 4 (2011) 3689–3696.
- Y. Chen, Y. Lin, Y. Zhang, S. Wang, D. Su, Z. Yang, M. Han, F. Chen, Low temperature solid oxide fuel cells with hierarchically porous cathode nano-network, *Nano Energy* 8 (2014) 25–33.
- Y. Zhang, Y. Li, T. Wu, W. Zhang, J. Zhu, Z. Li, J. Chen, B. Yu, J. Wang, J. Zhang, Oxygen reduction kinetics enhancements of intermediate-temperature SOFC cathodes with novel  $Nd_{0.5}Sr_{0.5}Co_{3-\delta}/Nd_{0.8}Sr_{1.2}Co_{4-\delta}$  heterointerfaces, *Nano Energy* 51 (2018) 711–720.
- S. Sengodan, Y.-W. Ju, O. Kwon, A. Jun, H.Y. Jeong, T. Ishihara, J. Shin, G. Kim, Self-decorated  $MnO$  nanoparticles on double perovskite solid oxide fuel cell anode by *in situ* exsolution, *ACS Sustain. Chem. Eng.* 5 (2017) 9207–9213.
- B. Hua, M. Li, Y.-F. Sun, Y.-Q. Zhang, N. Yan, J. Chen, T. Thundat, J. Li, J.-L. Luo, A coupling for success: controlled growth of  $Co/CoO_x$  nanosheets on perovskite mesoporous nanofibres as high-performance trifunctional electrocatalysts in alkaline condition, *Nano Energy* 32 (2017) 247–254.
- B. Hua, M. Li, Y.-F. Sun, J.-H. Li, J.-L. Luo, Enhancing perovskite electrocatalysis of solid oxide cells through controlled exsolution of nanoparticles, *ChemSusChem* 10 (2017) 3333–3341.
- J. Wang, F. Meng, T. Xia, Z. Shi, J. Lian, C. Xu, H. Zhao, J.-M. Bassat, J.-C. Grenier, Superior electrochemical performance and oxygen reduction kinetics of layered perovskite  $PrBa_xCo_2O_{5+\delta}$  ( $x = 0.90\text{--}1.0$ ) oxides as cathode materials for intermediate-temperature solid oxide fuel cells, *Int. J. Hydrogen Energy* 39 (2014) 18392–18404.
- Y. Zhang, R. Knibbe, J. Sunarso, Y. Zhong, W. Zhou, Z. Shao, Z. Zhu, Recent progress on advanced materials for solid-oxide fuel cells operating below 500 °C, *Adv. Mater.* 29 (2017) 1700132.
- Y. Chen, W. Zhou, D. Ding, M. Liu, F. Ciucci, M. Tade, Z. Shao, Advances in cathode materials for solid oxide fuel cells: complex oxides without alkaline earth metal elements, *Adv. Energy Mater.* 5 (2015) 1500537.
- J. Li, Q. Zhang, P. Qiu, L. Jia, B. Chi, J. Pu, J. Li, A  $CO_2$ -tolerant  $La_2NiO_{4+\delta}$ -coated  $PrBa_{0.5}Sr_{0.5}Co_{1.5}Fe_{0.5}O_{5+\delta}$  cathode for intermediate-temperature solid oxide fuel cells, *J. Power Sources* 342 (2017) 623–628.
- C. Su, X. Duan, J. Miao, Y. Zhong, W. Zhou, S. Wang, Z. Shao, Mixed conducting perovskite materials as superior catalysts for fast aqueous-phase advanced oxidation: a mechanism study, *ACS Catal.* 7 (2017) 388–397.
- R. Thalinger, M. Gocyla, M. Heggen, B. Klötzer, S. Penner, Exsolution of  $Fe$  and  $SrO$  nanorods and nanoparticles from lanthanum strontium ferrite  $La_{0.6}Sr_{0.4}FeO_{3-\delta}$  materials by hydrogen reduction, *J. Phys. Chem. C* 119 (2015) 22050–22056.
- R.T.K. Baker, R.J. Waite, Formation of Filamentous Carbon in Chemistry and Physics of Carbon, Marcel Dekker, New York, 1978, p. 83.
- K. Huang, L. Yuan, S. Feng, Crystal facet tailoring arts in perovskite oxides, *Inorg. Chem. Front.* 2 (2015) 965–981.
- S.B. Adler, J.A. Lane, B.C.H. Steele, Electrode kinetics of porous mixed-conducting oxygen electrodes, *J. Electrochem. Soc.* 143 (1996) 3554–3564.
- S.B. Adler, Factors governing oxygen reduction in solid oxide fuel cell cathodes, *Chem. Rev.* 104 (2004) 4791–4844.
- F. Mauvy, C. Lalanne, J.-M. Bassat, J.-C. Grenier, H. Zhao, L. Huo, P. Stevens, Electrode properties of  $Ln_2NiO_{4+\delta}$  ( $Ln = La, Nd, Pr$ ), *J. Electrochem. Soc.* 153 (2006) A1547–A1553.
- Z. Cai, M. Kubicek, J. Fleig, B. Yildiz, Chemical heterogeneities on  $La_{0.6}Sr_{0.4}CoO_{3-\delta}$  thin films—correlations to cathode surface activity and stability, *Chem. Mater.* 24

(2012) 1116–1127.

[45] Y. Liu, X. Zhu, M. Li, R.P. Ohaye, W. Yang, Nanoparticles at grain boundaries inhibit the phase transformation of perovskite membrane, *Nano Lett.* 15 (2015) 7678–7683.

[46] J.-D. Kim, G.-D. Kim, J.-W. Moon, Y.-I. Park, W.-H. Lee, K. Kobayashi, M. Nagai, C.-E. Kim, Characterization of LSM–YSZ composite electrode by ac impedance spectroscopy, *Solid State Ionics* 143 (2001) 379–389.

[47] A. Yan, V. Maragou, A. Arico, M. Cheng, P. Tsiaikaras, Investigation of a  $\text{Ba}_{0.5}\text{Sr}_{0.5}\text{Co}_{0.8}\text{Fe}_{0.2}\text{O}_{3-\delta}$  based cathode SOFC II. The effect of  $\text{CO}_2$  on the chemical stability, *Appl. Catal. B Environ.* 76 (2007) 320–327.

[48] F. Fang, N. Feng, L. Wang, J. Meng, G. Liu, P. Zhao, P. Gao, J. Ding, H. Wan, G. Guan, Fabrication of perovskite-type macro/mesoporous  $\text{La}_{1-x}\text{K}_x\text{FeO}_{3-\delta}$  nanotubes as an efficient catalyst for soot combustion, *Appl. Catal. B Environ.* 236 (2018) 184–194.

[49] L. Dong, Y. Tang, B. Li, L. Zhou, F. Gong, H. He, B. Sun, C. Tang, F. Gao, L. Dong, Influence of molar ratio and calcinations temperature on the properties of  $\text{Ti}_x\text{Sn}_{1-x}\text{O}_2$  supporting copper oxide for  $\text{CO}$  oxidation, *Appl. Catal. B Environ.* 180 (2016) 451–462.

[50] R. Zhang, A. Villanueva, H. Almandari, S. Kaliaguine, Catalytic reduction of  $\text{NO}$  by propene over  $\text{LaCo}_{1-x}\text{Cu}_x\text{O}_3$  perovskites synthesized by reactive grinding, *Appl. Catal. B Environ.* 64 (2006) 220–233.

[51] G. Zhang, Z. Liu, N. Zhu, W. Jiang, X. Dong, W. Jin, A novel  $\text{Nb}_2\text{O}_5$ -doped  $\text{SrCo}_{0.8}\text{Fe}_{0.2}\text{O}_{3-\delta}$  oxide with high permeability and stability for oxygen separation, *J. Membr. Sci.* (2012) 405–406 300–309.

[52] Jon A. Onrubia, B. Pereda-Ayo, U. De-La-Torre, Juan R. González, Velasco, Key factors in Sr-doped  $\text{LaBO}_3$  ( $\text{B} = \text{Co}$  or  $\text{Mn}$ ) perovskites for  $\text{NO}$  oxidation in efficient diesel exhaust purification, *Appl. Catal. B Environ.* 213 (2017) 198–210.

[53] H. Li, K. Yu, C. Wan, J. Zhu, X. Liu, S. Tong, Y. Zhao, Comparison of the nickel addition patterns on the catalytic performances of  $\text{LaCoO}_3$  for low-temperature  $\text{CO}$  oxidation, *Catal. Today* 281 (2017) 534–541.